

# Spin-Phonon Coupling Driven Charge Density Wave in a Kagome Magnet

H. Miao<sup>1,#</sup>, T. T. Zhang<sup>2</sup>, H. X. Li<sup>1,3</sup>, G. Fabbris<sup>4</sup>, A. H. Said<sup>4</sup>, R. Tartaglia<sup>4,5</sup>, T. Yilmaz<sup>6</sup>, E. Vescovo<sup>6</sup>, J.-X. Yin<sup>7</sup>, S. Murakami<sup>2</sup>, L. X. Feng<sup>8</sup>, K. Jiang<sup>8</sup>, X. L. Wu<sup>9</sup>, A. F. Wang<sup>9,#</sup>, S. Okamoto<sup>1,#</sup>, Y. L. Wang<sup>10,#</sup>, H. N. Lee<sup>1</sup>

<sup>1</sup>*Materials Science and Technology Division, Oak Ridge National Laboratory, Oak Ridge, Tennessee 37831, USA*

<sup>2</sup>*Department of Physics, Tokyo Institute of Technology, Okayama, Meguro-ku, Tokyo 152-8551, Japan*

<sup>3</sup>*Advanced Materials Thrust, The Hong Kong University of Science and Technology (Guangzhou), Guangzhou, Guangdong 511453, China.*

<sup>4</sup>*Advanced Photon Source, Argonne National Laboratory, Argonne, Illinois 60439, USA*

<sup>5</sup>*“Gleb Wataghin” Institute of Physics, University of Campinas, Campinas, São Paulo 13083-859, Brazil*

<sup>6</sup>*National Synchrotron Light Source II, Brookhaven National Laboratory, Upton, New York 11973, USA*

<sup>7</sup>*Laboratory for Quantum Emergence, Department of Physics, Southern University of Science and Technology, Shenzhen, Guangdong 518055, China.*

<sup>8</sup>*Beijing National Laboratory for Condensed Matter Physics, and Institute of Physics, Chinese Academy of Sciences, Beijing 100190, China*

<sup>9</sup>*Low Temperature Physics Laboratory, College of Physics and Center of Quantum Materials and Devices, Chongqing University, Chongqing 401331, China*

<sup>10</sup>*Hefei National Laboratory for Physical Science at Microscale, University of Science and Technology of China, Hefei, Anhui 230026, China*

**The intertwining between spin, charge, and lattice degrees of freedom can give rise to unusual macroscopic quantum states, including high-temperature superconductivity and quantum anomalous Hall effects. Recently, a charge density wave (CDW) is observed in the kagome antiferromagnet FeGe, indicative of possible intertwining physics. An outstanding question is that whether magnetic correlation is fundamental for the spontaneous spatial symmetry breaking orders. Here, utilizing elastic and high-resolution inelastic x-ray scattering, we discover a charge dimerization superlattice that coexists with the  $2\times 2\times 1$  CDW in the kagome sublattice. Most interestingly, between the magnetic and CDW transition temperature, the phonon dynamical structure factor shows a giant phonon-energy hardening and a substantial phonon linewidth broadening near the charge-dimerization**

**wavevectors, both signaling the spin-phonon coupling. By first principles calculations, we show that both the static and dynamic spin excitations intertwine with the phonon to drive the spatial symmetry breaking.**

The combination of magnetism and characteristic electronic structures of the kagome lattice, including flat-band<sup>1-3</sup>, Dirac-fermion<sup>4-7</sup> and van Hove singularities<sup>8,9</sup>, is a productive route to realize correlated and topological quantum states. Significant interests have been focused on a kagome superconductor  $AV_3Sb_5$  ( $A=K, Rb, Cs$ )<sup>10</sup>, where van Hove singularities near the Fermi level trigger cascade time- and spatial-symmetry breaking orders<sup>8-23</sup>. Lately, a strongly correlated version of  $AV_3Sb_5$  is realized in a kagome magnet  $FeGe$ <sup>24,25</sup>. Like the  $AV_3Sb_5$  ( $A=K, Rb, Cs$ )<sup>10</sup>, the electronic structure of  $FeGe$  features multiple van Hove singularities near the Fermi level,  $E_F$ <sup>24,25</sup>. A charge density wave (CDW) establishes in the A-type antiferromagnetic (A-AFM) phase and induces physical consequences, including anomalous Hall effect<sup>24</sup> and robust edge modes<sup>25</sup>, reminiscent to those observed in  $AV_3Sb_5$ <sup>16,18</sup>. Below the CDW transition temperature,  $T_{CDW}$ , the static spin polarization is enhanced, indicating an intimate correlation between spin, charge, and lattice degrees of freedom<sup>24</sup>. Despite these interesting observations, key questions yet to be answered. For instance, although CDW has been observed in correlated magnetic systems, such as the cuprate high- $T_c$  superconductors<sup>26,27</sup> and spin-density-wave systems<sup>28</sup>, emergence of CDW well below the magnetic transition temperature is rare, suggesting a new correlation driven CDW mechanism in  $FeGe$ . Focusing on the kagome metals with van Hove singularities near  $E_F$ , it is also urged to determine the geometry of the CDW in  $FeGe$  and its possible connection with the loop current scenario<sup>11-17,24</sup>. Here, we address these fundamental questions using advanced x-ray scattering and numerical calculations. We discover charge-dimerization superlattice peaks at the A-AFM wavevectors in  $FeGe$ , differentiating the CDW geometry in  $FeGe$  and  $AV_3Sb_5$  despite the same  $2\times 2\times 2$  superstructure<sup>20</sup>. Most interestingly, the phonon dynamical structure factor shows giant phonon hardening and large phonon broadening effect near the charge-dimerization wavevectors above the  $T_{CDW}$ . These phonon anomalies are in stark contrast with the phonon softening, known as Kohn anomaly, in the electron-phonon coupled systems and the emergent amplitude mode that hardens below the  $T_{CDW}$ <sup>19</sup>. Combining with density-functional theory (DFT) and model calculations, we prove that the charge-dimerized  $2\times 2\times 2$  superstructure with  $P6/mmm$

space group is an energetically favored ground state that is stabilized by the strong spin-phonon interactions.

FeGe adopts a hexagonal structure with space group  $P6/mmm$  (No. 191). It is composed of a kagome lattice of Fe atoms with Ge-1 centered in the hexagons. These kagome layers are stacked along the c-axis and separated by honeycomb layers of Ge-2. At  $T_N=410$  K, an A-AFM kicks in with spin moment pointing along the c-axis. Below  $T_{CDW}\sim 110$  K, concomitant anomalous Hall effect and enhanced spin polarization are observed<sup>24</sup>. Figure 1b shows the density functional theory plus dynamical mean field theory (DFT+DMFT) calculated spectral function of FeGe. In agreement with angle-resolved photoemission spectroscopy (ARPES) study<sup>24</sup>, van Hove singularities at the  $\mathbf{M}$  point (Fig. 1c) are pushed to the Fermi-level due to the local correlation effect (see also the supplementary materials). Figure 1d and 1e show x-ray diffraction scans along high-symmetry directions at  $T=10$  K. Consistent with previous diffraction and scanning tunneling microscopy studies<sup>24,25</sup>, CDW superlattice peaks are observed at  $Q_M^{\parallel}$  ( $H=0.5, K, L=\text{integer}$ ) and  $Q_L$  ( $H=0.5, K, L=\text{integer}+0.5$ ), where  $H, K, L$  are reciprocal lattice directions as shown in Fig. 1c (see supplementary materials for more  $\mathbf{Q}$  positions). While superlattice peak positions at  $Q_M^{\parallel}$  and  $Q_L$  are the same as  $AV_3Sb_5$ <sup>19,20,22</sup>, as shown in Fig. 1e, we observe a new superlattice peak at  $Q_A^{\perp}=(0, 0, 2.5)$  that is absent in  $AV_3Sb_5$ <sup>19</sup>. This new superlattice peak is narrow with a half-width-at-half-maximum (HWHM) $\sim 0.001$  in reciprocal lattice units and doubles the unit cell along the crystal c-axis.

Since  $Q_A^{\perp}=(0, 0, L=\text{half-integer})$  overlaps with the A-type AFM peaks, it is necessary to prove that the observed peak at  $Q_A^{\perp}$  is not due to the magnetic cross-section of x-ray scattering. For this purpose, we determine the temperature dependent superlattice peaks at  $Q_L=(0, 0.5, 2.5)$ ,  $Q_M^{\parallel}=(0, 0.5, 3)$  and  $Q_A^{\perp}=(0, 0, 2.5)$  and  $(0, 0, 4.5)$ . Figures 2 a,c,e show  $\theta-2\theta$  scans below (90 K) and above (116 K)  $T_{CDW}$ . Figures 2 b,d,f show the full temperature dependent peak intensities and peak widths across the  $T_{CDW}$ . The same onset temperature for all four wave-vectors proves that  $Q_A^{\perp}$  peaks correspond to charge superlattice along the c-axis. Since the x-ray scattering amplitude at  $\mathbf{Q}=(0, 0, L)$  probes lattice distortions along the c-axis, the superlattice peaks at  $Q_A^{\perp}$  demonstrate the emergence of charge-dimerization below  $T_{CDW}$ . Insets of Fig. 2b and 2d show the hysteresis-scans

at  $Q_L$  and  $Q_M^{\prime\prime}$  near  $T_{\text{CDW}}$ . The small hysteresis temperature,  $\Delta T \sim 0.5$  K, indicates that the transition at  $T_{\text{CDW}}$  is a weak first-order transition. We note that we do not observe the temperature dependent hysteresis at  $Q_A^\perp$ , possibly due to its relatively weak peak intensity near  $T_{\text{CDW}}$  and even smaller hysteresis temperature,  $\Delta T$ . Given both  $Q_A^\perp$  and  $Q_M^{\prime\prime}$  are present in FeGe, the  $2 \times 2 \times 2$  superstructure peaks at  $Q_L$  should be considered as a superposition of charge dimerization at  $Q_A^\perp$  and  $2 \times 2 \times 1$  CDW at the three-equivalent  $Q_M^{\prime\prime}$ . An important consequence of the charge-dimerization superlattice peak is that it distinguishes the  $2 \times 2 \times 2$  charge modulations in FeGe and  $\text{AV}_3\text{Sb}_5$ , pointing to different electronic and structural origin of the CDWs in these two kagome metals.

The observation of charge-dimerization superlattice peaks on top of the A-AFM peaks naturally indicate a spin-phonon interaction in FeGe. We thus turn to determine the phonon dynamical structure factor,  $S(\mathbf{Q}, \omega)$ , using meV-resolution inelastic x-ray scattering (IXS). Figure 3a and b show experimental and DFT calculated  $S(\mathbf{Q}, \omega)$  along the  $\Gamma(0, 0, 4)$ - $\mathbf{M}(0.5, 0, 4)$ - $\mathbf{L}(0.5, 0, 4.5)$ - $\mathbf{A}(0, 0, 4.5)$ - $\Gamma(0, 0, 4)$  direction at 200 K. The overall agreements between IXS and DFT, including the phonon dispersion and intensity distribution, are good. However, we find that the phonon peak-widths near  $Q_A^\perp$  are unusually broad, suggesting quasiparticle interactions<sup>29-33</sup>. To reveal more details of this phonon anomaly, in Fig. 3c, we show the phonon band dispersion at 200 and 420 K and the extracted phonon peak width at 200 K along the  $\mathbf{M}$ - $\Gamma$ - $\mathbf{A}$  direction. Interestingly, the phonon energy at the  $\mathbf{A}$ -point shows over 10% hardening effect from 420 to 200 K that accompanies with a phonon linewidth broadening. Fig. 3d and e show representative temperature dependent IXS spectra at the  $\mathbf{M}$  and  $\mathbf{A}$  point, respectively. The full temperature dependence of the extracted peak positions is shown in Fig. 3f. We find that the phonon peaks at the  $\mathbf{M}$  point remain temperature independent within experimental error, whereas the phonon mode at the  $\mathbf{A}$  point shows a giant 14% hardening from 420 to 110 K. Figure 3g summarizes the temperature dependent phonon width at the  $\mathbf{A}$  and  $\mathbf{M}$  point. The extracted phonon peak-width at the  $\mathbf{A}$ -point is broad even above the  $T_N$  with  $\text{HWHM} \sim 0.4$  meV. The width continuously increases until temperature hits the  $T_{\text{CDW}}$ . At  $T = 150$  K, the extracted  $\text{HWHM} \sim 1$  meV, corresponding to a dimpling ratio  $\sim 7\%$ . In stark contrast, the extracted phonon peak width at the  $\mathbf{M}$  point is less than 0.1 meV in the entire temperature range, consistent with the absence of phonon energy anomaly at the  $\mathbf{M}$ -point (Note that the  $\text{HWHM}$

shown in Fig. 3g is the intrinsic peak width without resolution broadening effect, see method for fitting details).

The observed phonon hardening and broadening above the  $T_{\text{CDW}}$  in FeGe are fundamentally different from the Kohn anomaly in electron-phonon coupled CDW systems and the emergent amplitude mode below the  $T_{\text{CDW}}$ <sup>19,29-31</sup>. These phonon anomalies are, however, captured by the spin-phonon coupling picture shown in Fig. 3h. The second order Feynman diagram depicts a phonon with energy,  $\omega_n$ , and momentum,  $q$ , scatters into two magnons with  $(\xi_m, k)$  and  $(\omega_n - \xi_m, q - k)$ . As we show in more details in the Supplementary Materials, this dynamical spin-phonon interaction yields strong phonon self-energy effect, including the phonon energy hardening and phonon linewidth broadening near the A-point, in agreement with experimental observations. Interestingly, similar phonon anomalies induced by the spin-phonon interaction have also been observed in FeSi, where the magnitude of phonon energy hardening and lifetime damping are close to our observations<sup>33</sup>. The discovery of charge-dimerization superlattice peaks and the associated giant phonon anomalies constitute our main experimental observations.

Motivated by these experimental results, we perform DFT+ $U$  calculations for the A-AFM phase of FeGe at the zero temperature to understand the role of electronic correlations and static spin-polarizations in driving the charge-dimerized  $2 \times 2 \times 2$  superstructure. Figure 4a-c show the calculated phonon spectra of FeGe in the A-AFM phase as increasing Hubbard  $U$ . We find that the experimentally observed phonon modes shown in Fig. 3a exhibit the most dramatic change as increasing  $U$  with an energy minimum at the **L** point for  $U < 2$  eV. This observation indicates that stronger electronic correlations and spin-polarizations tend to induce a lattice instability in FeGe. Interestingly, this mode corresponds to atomic vibrations that are mainly composed of out-of-phase c-axis lattice distortions between adjacent Fe-Ge kagome layers, consistent with experimentally observed charge-dimerization peaks. To understand the nature of the  $2 \times 2 \times 2$  superstructure, we take the equal phase and amplitude superpositions of the experimentally observed phonon mode at the three equivalent **L**-points as shown in Fig. 4d. The arrows point the movement of Fe and Ge atoms. In kagome layers, Fe and Ge atoms move out-of-plane to form charge-dimers along the c-axis. The Ge-1 atoms are divided into out-of-phase Ge-1a (blue) and Ge-1b (light blue) groups, where Ge-1a has a larger atomic movement than that of Ge-1b. The honeycomb layers of Ge-2

atoms (grey) show in-plane Kekulé-type distortions<sup>34,35</sup>. Starting from this  $2\times 2\times 2$  supercell that preserves the  $P6/mmm$  space group, we relax the internal atomic positions. Figure 4e shows the energy difference between the charge-dimerized  $2\times 2\times 2$  superstructure and the ideal kagome phase,  $\Delta E = E_{Charge-Dimer} - E_{Kagome}$ , which decreases as increasing  $U$ . Intriguingly, the charge-dimerized  $2\times 2\times 2$  superstructure is already an energetically favored phase at  $U=0$  and becomes even more robust with increasing  $U$  accompanied by the increase in the static moment. These results prove that the magnitude of the static spin-polarization is critical to stabilize the charge dimerized  $2\times 2\times 2$  superstructure. Furthermore, as we show in Fig. 4e, by forming the charge-dimerized  $2\times 2\times 2$  superstructure, the ordered magnetic moment is further enhanced by  $0.01\sim 0.05 \mu_B/\text{Fe}$  at  $U=0\sim 3\text{eV}$ , consistent with the previous neutron scattering study<sup>24</sup>.

Our experimental and numerical results establish a spin-phonon coupling picture for the emergence of CDW in FeGe. Near  $T_{CDW}$ , the energy gain by forming a charge-dimerized  $2\times 2\times 2$  superstructure with enhanced static moment overcomes the energy cost of lattice distortions and gives rise to a weak first order phase transition<sup>36</sup>. This process is reminiscent to the spin-Peierls transition in a 1-dimensional spin-chain<sup>37</sup>. However, in FeGe the presence of large itinerant electrons allows additional energy gain by enlarging the spin polarization and removing the high density-of-states near  $E_F$ . The competing magnetic, lattice and charge energy scales make a complex landscape of symmetry breaking orders in kagome magnet FeGe.

## Methods

### Sample preparation and characterizations

Single crystals of B35-type FeGe were grown via chemical vapor transport method. Stoichiometric iron powders (99.99%) and germanium powders (99.999%) were mixed and sealed in an evacuated quartz tube with additional iodine as the transport agent. The quartz tube was then loaded into a two-zone horizontal furnace with a temperature gradient from 600 °C (source) to 550 °C (sink). After 12 days growth, FeGe single crystals with typical size  $1.5\times 1.5\times 3 \text{ mm}^3$  can be obtained in the middle of the quartz tube.

### Elastic X-ray scattering

The single crystal elastic X-ray diffraction was performed at the 4-ID-D beamline of the Advanced Photon Source (APS), Argonne National Laboratory (ANL). The incident photon energy was set to 11 keV, slightly below the Ge K-edge to reduce the fluorescence background. The X-rays higher harmonics were suppressed using a Si mirror and by detuning the Si (111) monochromator. Diffraction was measured using a vertical scattering plane geometry and horizontally polarized ( $\sigma$ ) X-rays. The incident intensity was monitored by a He filled ion chamber, while diffraction

was collected using a Si-drift energy dispersive detector with approximately 200 eV energy resolution. The sample temperature was controlled using a He closed cycle cryostat and oriented such that X-rays scattered from the (001) surface.

### meV-resolution inelastic X-ray scattering

The experiments were conducted at beam line 30-ID-C (HERIX) at APS, ANL<sup>38</sup>. The highly monochromatic x-ray beam of incident energy  $E_i = 23.7$  keV ( $\lambda = 0.5226$  Å) was focused on the sample with a beam cross section of  $\sim 35 \times 15$   $\mu\text{m}^2$  (horizontal  $\times$  vertical). The overall energy resolution of the HERIX spectrometer was  $\Delta E \sim 1.5$  meV (full width at half maximum). The measurements were performed in reflection geometry. Under this geometry, IXS is primarily sensitive the lattice distortions along the crystal c-axis. This geometry selectively enhances the unstable phonon modes predicted in the DFT calculations. Typical counting times were in the range of 120 to 240 seconds per point in the energy scans at constant momentum transfer  $\mathbf{Q}$ .  $H$ ,  $K$ ,  $L$  are defined in the hexagonal structure with  $a=b=4.97$  Å,  $c=4.04$  Å at the room temperature.

### Curve Fitting

The total energy resolution  $\Delta E = 1.5$  meV is calibrated by fitting the elastic peak to a pseudo-voigt function:

$$R(\omega) = (1 - \alpha) \frac{1}{\sqrt{2\pi}\sigma} e^{-\frac{\omega}{2\sigma^2}} + \alpha \frac{1}{\pi} \frac{\Gamma}{\omega^2 + \Gamma^2} \quad (\text{M1})$$

where the energy resolution is the FWHM.

IXS directly probes the phonon dynamical structure factor,  $S(\mathbf{Q}, \omega)$ . The IXS cross-section for solid angle  $d\Omega$  and bandwidth  $d\omega$  can be expressed as:

$$\frac{d^2\sigma}{d\Omega d\omega} = \frac{k_f}{k_i} r_0^2 |\vec{\epsilon}_i \cdot \vec{\epsilon}_f|^2 S(\mathbf{Q}, \omega) \quad (\text{M2})$$

where  $\mathbf{k}$  and  $\boldsymbol{\epsilon}$  represent the scattering vector and x-ray polarization and  $i$  and  $f$  denote initial and final states.  $r_0$  is the classical radius of the electron. In a typical measurement, the energy transfer  $\omega$  is much smaller than the incident photon energy (23.71 keV in our study). Therefore, the term  $\frac{k_f}{k_i} \sim 1$ , and  $\frac{d^2\sigma}{d\Omega d\omega} \propto S(\mathbf{Q}, \omega)$ .

$S(\mathbf{Q}, \omega)$  is related to the imaginary part of the dynamical susceptibility,  $\chi''(\mathbf{Q}, \omega)$ , through the fluctuation-dissipation theorem:

$$S(\mathbf{Q}, \omega) = \frac{1}{\pi} \frac{1}{(1 - e^{\omega/k_B T})} \chi''(\mathbf{Q}, \omega) \quad (\text{M3})$$

Where  $\chi''(\mathbf{Q}, \omega)$  can be described by the damped harmonic oscillator form, which has antisymmetric Lorentzian lineshape:

$$\chi''(\mathbf{Q}, \omega) = \sum_i I_i \left[ \frac{\Gamma_i}{(\omega - \omega_{\mathbf{Q},i})^2 + \Gamma_i^2} - \frac{\Gamma_i}{(\omega + \omega_{\mathbf{Q},i})^2 + \Gamma_i^2} \right] \quad (\text{M4})$$

here  $i$  indexes the different phonon peaks.

The phonon peak can be extracted by fitting the IXS spectrum at constant-momentum transfer  $\mathbf{Q}$ , using Eq. (M3) and (M4). Due to the finite experimental resolution, the IXS intensity is a convolution of  $S(\mathbf{Q}, \omega)$  and the instrumental resolution function,  $R(\omega)$ :

$$I(\mathbf{Q}, \omega) = S(\mathbf{Q}, \omega) \otimes R(\omega) \quad (\text{M5})$$

Here  $R(\omega)$  was determined by fitting of the elastic peak.

## ARPES experiment

The ARPES experiments are performed on single crystals FeGe. The samples are cleaved in situ in a vacuum better than  $5 \times 10^{-11}$  torr. The experiment is performed at beam line 21-ID-1 at the NSLS-II. The measurements are taken with synchrotron light source and a Scienta-Omicron DA30 electron analyzer. The total energy resolution of the ARPES measurement is approximately 15 meV. The sample stage is maintained at  $T=30$  K throughout the experiment.

## DFT+U calculations

DFT+U calculations are performed using Vienna ab initio simulation package (VASP)<sup>39</sup>. The exchange-correlation potential is treated within the generalized gradient approximation (GGA) of the Perdew-Burke-Ernzerhof variety<sup>40</sup>. The simplified approach introduced by Dudarev et al. (LDAUTYPE=2) is used<sup>41</sup>. We used experimental lattice parameters of FeGe and FeSn<sup>24,42</sup>. Phonon calculations are performed in the A-type AFM phase with a  $2 \times 2 \times 1$  supercell (with respect to the AFM cell), using both the density-functional-perturbation theory (DFPT)<sup>43</sup> and frozen phonon approaches, combined with the *Phonopy* package<sup>44</sup>. The two approaches yield identical results. The internal atomic positions of the charge-dimerized  $2 \times 2 \times 2$  superstructure is relaxed with the initial atomic distortions shown in Fig. 4d, until the force is less than 0.001 eV/Å for each atom. Integration for the Brillouin zone is done using a  $\Gamma$ -centered  $8 \times 8 \times 10$   $k$ -point grids for the  $2 \times 2 \times 2$  supercell and the cutoff energy for plane-wave-basis is set to be 500 eV.

## DFT+DMFT calculations

The fully charge self-consistent DFT+DMFT<sup>45</sup> calculations are performed in the A-type AFM phase using an open-source code of DFT+embedded DMFT developed by Haule et al., based on Wien2k package<sup>46</sup>. We choose a hybridization energy window from -10 eV to 10 eV with respect to the Fermi level. All the five  $3d$  orbitals on an Fe site are considered as correlated ones and a local Coulomb interaction Hamiltonian of Ising form is applied with varied Hubbard  $U$  and Hund's coupling  $J_H$  shown in the main text. The continuous time quantum Monte Carlo<sup>47</sup> is used as the impurity solver. We choose an "exact" double counting scheme invented by Haule<sup>48</sup>. The self-energy on real frequencies is obtained by the analytical continuation method of maximum entropy. The SOC is not included in the DFT+DMFT calculations since the SOC strength of Fe- $3d$  orbitals is small and will rarely change the electronic correlations. All the calculations are performed at  $T=80$  K.

**Data availability:** The data that support the findings of this study are available from the corresponding author on reasonable request.

**Acknowledgements:** We thank Matthew Brahlek, Pengcheng Dai, Jiangping Hu, H. C. Lei, Brain Sales, Jiaqiang Yan, Jiaxin Yin, Binghai Yan, Ming Yi, Zhida Song and Jianzhou Zhao for stimulating discussions. This research was supported by the U.S. Department of Energy, Office of Science, Basic Energy Sciences, Materials Sciences and Engineering Division (x-ray and ARPES measurement and model analysis). This research used resources (beamline 4ID and 30ID) of the Advanced Photon Source, a U.S. DOE Office of Science User Facility operated for the DOE Office of Science by Argonne National Laboratory under Contract No. DE-AC02-06CH11357. ARPES measurements used resources at 21-ID-1 beamlines of the National Synchrotron Light Source II, a US Department of Energy Office of Science User Facility operated for the DOE Office of Science by Brookhaven National Laboratory under contract



no. DE-SC0012704. T.T. Z. and S. M. acknowledge support from Tokodai Institute for Element Strategy (TIES) funded by MEXT Elements Strategy Initiative to Form Core Research Center Grants No. JPMXP0112101001, JP18J23289, JP18H03678, and JP22H00108. X.L.W. and A.F.W. acknowledge the support by the National Natural Science Foundation of China (Grant No. 12004056). T.T. Z. also acknowledge the support by Japan Society for the Promotion of Science (JSPS), KAKENHI Grant No. JP21K13865. Y.L.W. acknowledge the support by USTC Research Funds of the Double First-Class Initiative (No. YD2340002005). The DFT and DFT+DMFT calculations were performed on TianHe-1A, the National Supercomputer Center in Tianjin, China. R. T. acknowledge the support from The São Paulo Research Foundation, FAPESP (Grant No. 2021/11170-0).

### **Author Contributions:**

H.M., H.X.L, G.F., R.S. performed the elastic x-ray scattering measurement. H.M., H.X.L., G.F., A.S. performed the inelastic x-ray scattering. H.M., H.X.L., H.N.L., T.Y., E.V. performed the ARPES measurement. X.L.W. and A.F.W. grew the single crystals of FeGe. T.T.Z. and S.M. calculated the phonon dynamical structure factor. Y.L.W. performed DFT+U and DFT+DMFT calculations for FeGe and FeSn. L.X.F., K.J. and S.O. performed the 1D model Analysis. H.M., T.T.Z., S.O. and Y.L.W. wrote the paper with inputs from all co-authors.

**Competing interest:** The authors declare no competing interests.

### **References:**

1. Tang, E., Mei, J. W. and Wen, X.-G. High-Temperature Fractional Quantum Hall States, *Phys. Rev. Lett.* **106**, 236802 (2012).
2. Okamoto, S. *et al.*, Topological flat bands in a Kagome lattice multiorbital system. *Communications Physics* **5**:198 (2022).
3. Kang, M *et al.*, Dirac fermions and flat bands in the ideal Kagome metal FeSn, *Nat. Mater.* **19**, 163-169 (2020).
4. Ye, L. D. *et al.*, Massive Dirac fermions in a ferromagnetic Kagome metal, *Nature* **555**, 638-642 (2018).
5. Liu, D. F. *et al.*, Magnetic Weyl semimetal phase in a Kagome crystal, *Science* **365**, 1282-1285 (2019).
6. Yin, J.-X., Pan, S. H. and Hasan, M. Z. Probing topological quantum matter with scanning tunnelling microscopy, *Nat. Rev. Phys* **3**, 249 (2021).
7. Yin, J. X. *et al.*, Quantum-limit Chern topological magnetism in TbMn<sub>6</sub>Sn<sub>6</sub>, *Nature* **583**, 533-536 (2020).
8. Wang, W.-S., Li, Z.-Z., Xiang, Y.-Y. and Wang, Q.-H. Competing electronic orders on kagome lattices at van hove filling, *Phys. Rev. B* **87**, 115135 (2013).
9. Kiesel, M. L., Platt, C. and Thomale, R. Unconventional fermi surface instabilities in the kagome hubbard model, *Phys. Rev. Lett.* **110**, 126405 (2013).
10. Ortiz, B. R. *et al.*, CsV<sub>3</sub>Sb<sub>5</sub>: A Z<sub>2</sub> Topological Kagome Metal with a Superconducting Ground State, *Phys. Rev. Lett.* **125**, 247002 (2020).

11. Feng, X., Jiang, K., Wang, Z. and Hu, J. P., Chiral flux phase in the kagome superconductor  $AV_3Sb_5$ , *Sci. Bull.* **66**, 1384 (2021).
12. Denner, M. M., Thomaly, R. and Neupert, T., Analysis of Charge Order in the Kagome Metal  $AV_3Sb_5$  ( $A=K, Rb, Cs$ ), *Phys. Rev. Lett.* **127**, 217601 (2021).
13. Lin, Y. P. and Nandkishore, R. M., Complex charge density waves at van Hove singularity on hexagonal lattices: Haldane-model phase diagram and potential realization in kagome metals  $AV_3Sb_5$ , *Phys. Rev. B* **104**, 045122 (2021).
14. Park, T., Ye, M. and Balents, L., Electronic instabilities of kagome metals: Saddle points and Landau theory, *Phys. Rev. B* **104**, 035142 (2021).
15. Christensen, M. H., Birol, T., Andersen, B. M. and Fernandes, R. M. Theory of the charge density wave in  $AV_3Sb_5$  kagome metals, *Phys. Rev. B* **104**, 214513 (2021).
16. Jiang, Y.-X. *et al.* Unconventional chiral charge order in kagome superconductor  $KV_3Sb_5$ , *Nat. Mater.* 10.1038/s41563-021-01034-y (2021).
17. Mielke III, C. *et al.* Time-reversal symmetry-breaking charge order in a kagome superconductor, *Nature* **502**, 245–250 (2022).
18. Yang, S.-Y. *et al.* Giant, unconventional anomalous Hall effect in the metallic frustrated magnet candidate,  $KV_3Sb_5$ , *Sci. Adv.* **6**, 10.1126/sci-adv.abb6003 (2020).
19. Li, H. *et al.*, Observation of Unconventional Charge Density Wave without Acoustic Phonon Anomaly in Kagome Superconductors  $AV_3Sb_5$ , *Phys. Rev. X* **11**, 031050 (2021).
20. Miao, H. *et al.*, Geometry of the charge density wave in the kagome metal  $AV_3Sb_5$ , *Phys. Rev. B* **104**, 195132 (2021).
21. Zhao, H. *et al.*, Cascade of correlated electron states in the kagome superconductor  $CsV_3Sb_5$ . *Nature* **599**, 216-221 (2021).
22. Nie, L. *et al.*, Charge-density-wave driven electronic nematicity in a kagome superconductor. *Nature* **604**, 59-64 (2022).
23. Li, H. *et al.*, Discovery of conjoined charge density waves in the kagome superconductor  $CsV_3Sb_5$ , *Nat. Commun.* **13**:6348 (2022).
24. Teng, X. *et al.*, Discovery of charge density wave in a correlated Kagome lattice antiferromagnet, *Nature* **609**, 490-495 (2022).
25. Yin, J. X. *et al.*, Discovery of charge order and corresponding edge state in Kagome magnet  $FeGe$ , *Phys. Rev. Lett.* **129**, 166401 (2022).
26. Tranquada, J. *et al.*, Evidence of stripe correlations of spins and holes in copper oxide superconductor. *Nature* **375**, 561-563 (1995).

27. Miao, H. *et al.*, High-temperature charge density wave correlations in  $\text{La}_{1.875}\text{Ba}_{0.125}\text{CuO}_4$  without spin-charge locking. *Proc. Natl. Acad. Sci. U. S. A.* **114**, 12430 (2017).
28. Hill, J., Helgesen, G. and Gibbs, D. X-ray scattering study of charge- and spin-density waves in chromium. *Phys. Rev. B* **51**, 10336 (1995).
29. M. Hoesch, A. Bosak, D. Chernyshov, H. Berger, and M. Krisch, Giant Kohn Anomaly and the Phase Transition in Charge Density Wave  $\text{ZrTe}_3$ , *Phys. Rev. Lett.* **102**, 086402 (2009).
30. Weber, F. *et al.*, Extended phonon collapse and the origin of the charge-density wave in  $2\text{H-NbSe}_2$ . *Phys. Rev. Lett.* **107**, 107403 (2011).
31. Miao, H. *et al.*, Incommensurate phonon anomaly and the nature of charge density waves in cuprates. *Phys. Rev. X* **8**, 011008 (2018).
32. Li, H *et al.*, Giant phonon anomalies in the proximate Kitaev quantum spin liquid  $\alpha\text{-RuCl}_3$ . *Nat. Commun.* 12:3513 (2021).
33. Krannich, S. *et al.*, Magnetic moments induced strong phonon renormalization in  $\text{FeSi}$ , *Nat. Commun.* **6**:8961 (2015).
34. Kekulé, A. Studies on aromatic compounds. *Ann. Chem. Pharm.* **137**, 129 (1865).
35. Shao, S. *et al.*, Charge density wave interaction in a Kagome-honeycomb antiferromagnet. arXiv: 2206.12033.
36. Binder, K. Theory of first-order phase transitions. *Rep. Prog. Phys.* **50**, 783 (1987).
37. Pytte, E. Peierls instability in Heisenberg chains. *Phys. Rev. B* **10**, 4637 (1974).
38. Toellner, T., Alatas, A. and Said, A. Six-reflection meV-monochromator for synchrotron radiation. *Journal of Synchrotron Radiation* **18**, 605 (2011).
39. Kresse, G. and Furthmüller, J. Efficient iterative schemes for ab initio total-energy calculations using a plane-wave basis set. *Phys. Rev. B* **54**, 11169 (1996).
40. Perdew, J. P., Burke, K. and Ernzerhof, M. Generalized gradient approximation made simple. *Phys. Rev. Lett.* **77**, 3865 (1996).
41. Dudarev, S. L., Botton, G. A., Savrasov, S. Y., Humphreys, C. J. and Sutton, A. P. Electron-energy-loss spectra and the structural stability of nickel oxide: an LSDA+U study. *Phys. Rev. B* **57**, 1505 (1998).
42. Meier, W. R. *et al.*, flat bands in the  $\text{CoSn}$ -type compounds. *Phys. Rev. B* **102**, 075148 (2020).
43. Donze, X. and Lee, C. Dynamical matrices, Born effective charges, dielectric permittivity tensors, and interatomic force constants from density-functional perturbation theory. *Phys. Rev. B* **55**, 10355 (1997).
44. Togo, A. and Tanaka, I. First principles phonon calculations in materials science. *Scr. Mater.* **108**, 1-5 (2015).

45. Georges, A. et al., Dynamical mean-field theory of strongly correlated fermion systems and the limit of infinite dimensions. *Rev. Mod. Phys.* **68**, 13 (1996).
46. Haule, K., Yee, C.-H. and Kim, K. Dynamical mean-field theory within the full-potential methods: electronic structure of CeIrIn<sub>5</sub>, CeCoIn<sub>5</sub>, and CeRhIn<sub>5</sub>. *Phys. Rev. B* **81**, 195107 (2010).
47. Gull, E. et al., Continuous-time Monte Carlo methods for quantum impurity models. *Rev. Mod. Phys.* **83**, 349 (2011).
48. Haule, K. Exact double counting in combining the dynamical mean field theory and the density functional theory. *Phys. Rev. Lett.* **115**, 196403 (2015).
49. Miao, H. et al., Observation of double Weyl phonons in parity-breaking FeSi. *Phys. Rev. Lett.* **121**, 035302 (2018).
50. Li, H. X. et al., Observation of a chiral wave function in the twofold-degenerate quadruple Weyl system BaPtGe. *Phys. Rev. B* **103**, 184301 (2021).

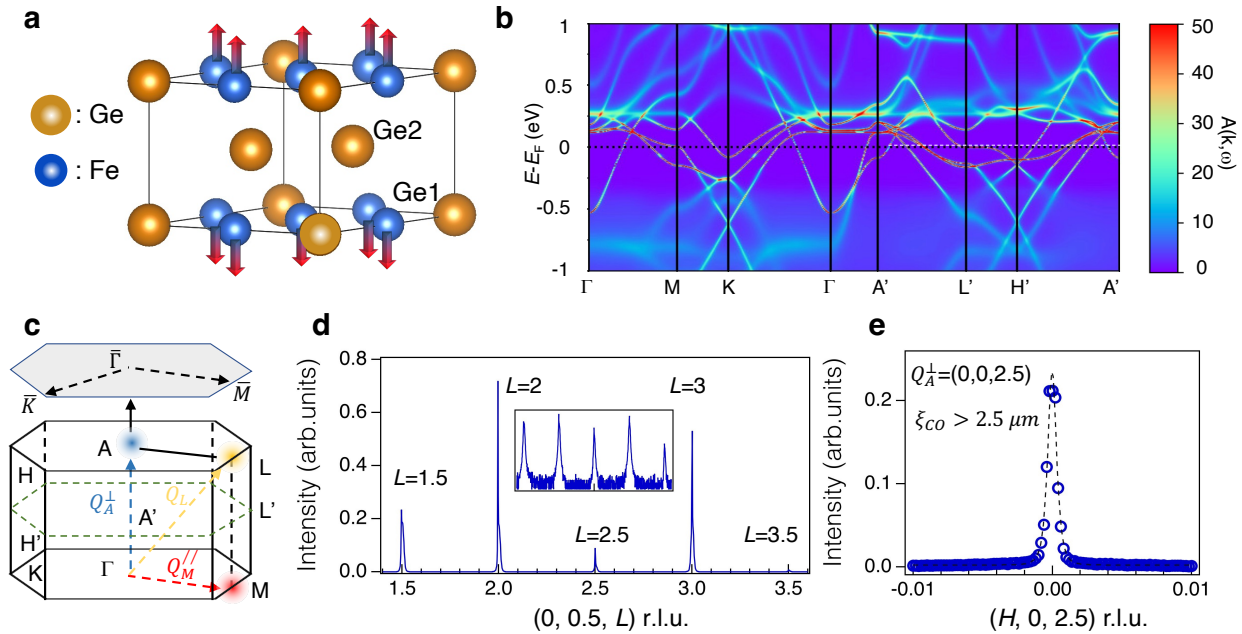


**Figure 1: Spin, charge, and lattice structures of FeGe.** **a**, Crystal and magnetic structure of FeGe. **b**, DFT+DMFT calculated electronic structure in the A-AFM phase with  $U=4.2$  eV and  $J_H=0.88$  eV showing van Hove singularities near the Fermi level, consistent with experiment<sup>24</sup>. **c**, High symmetry points and directions in the non-magnetic bulk and surface (grey hexagon) Brillouin zone. Since the magnetic unit cell doubles the non-magnetic unit cell along the  $\Gamma$ -A direction, the magnetic Brillouin zone is half of the non-magnetic Brillouin zone along the  $\Gamma$ -A

direction (green dashed lines).  $Q_A^\perp$  and  $Q_M^{\parallel}$  are corresponding to the charge-dimer and van Hove singularity nesting wavevectors, respectively. As discussed in the main text,  $Q_L$  is naturally described as a superposition of  $Q_A^\perp$  and  $Q_M^{\parallel}$ . **d**,  $L$ -scan along the  $[0, 0.5, L]$  direction. The inset shows the same intensity in log-scale. **e**,  $H$ -scan at charge-dimer wavevector  $(0, 0, 2.5)$ . The dashed curve is a fitting of the peak using Lorentzian-squared function. Data shown in **d** and **e** were taken at 10 K.

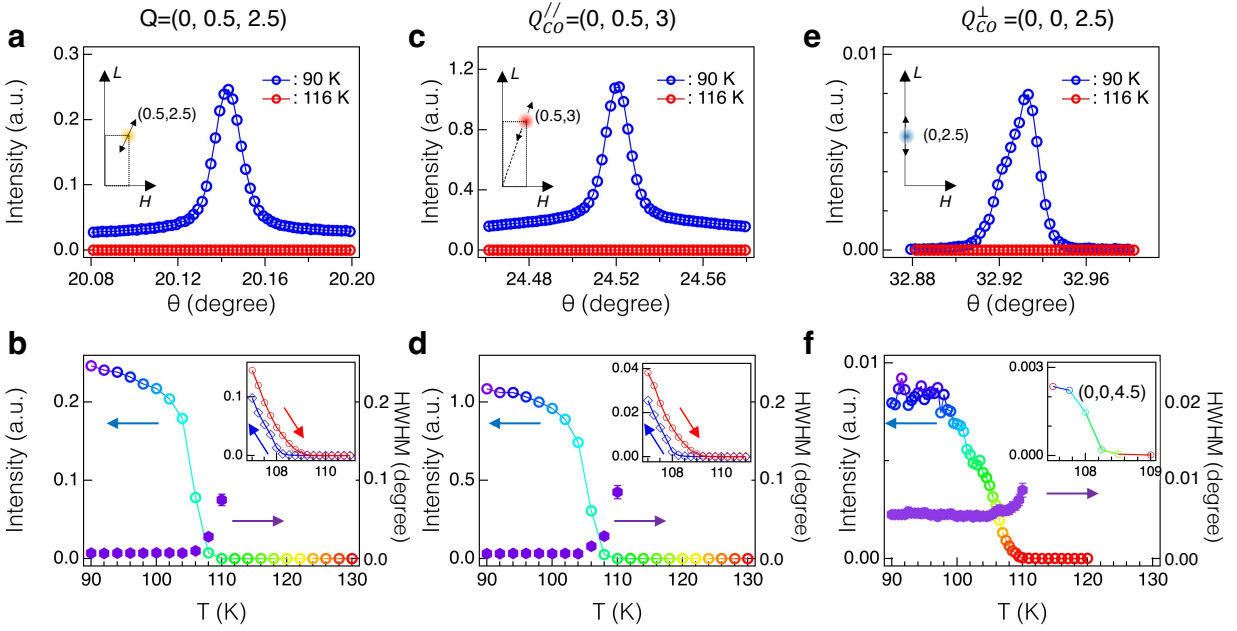


**Figure 2: Observation of charge dimerization superlattice peaks.** **a, c, e**,  $\theta$ - $2\theta$  scans at  $Q=(0, 0.5, 2.5)$ ,  $(0, 0.5, 3)$  and  $(0, 0, 2.5)$ . Their corresponding trajectories in the momentum space are shown in the inset of **a, c, e**. Red and blue curves correspond to scans at  $T = 116$  and  $90$  K, respectively. The temperature dependent peak intensities at  $Q_L=(0, 0.5, 2.5)$ ,  $Q_M^{\parallel}=(0, 0.5, 3)$  and  $Q_A^\perp=(0, 0, 2.5)$  are shown in **b, d**, and **f**, respectively. The color scheme in **b, d** and **f** highlights the temperature evolution of the data point. Open and solid marks represent peak intensity and peak width, respectively. Insets of **b** and **d** show hysteresis scans of the peak intensity near  $T_{CDW}$ , uncovering a weak first order phase transition. The inset of **f** shows the temperature dependent peak intensity at another charge-dimer wavevector  $(0, 0, 4.5)$ . All experimental data except the inset of **f** were collected at 4-ID, APS with photon energy  $h\nu=11$  keV. The data shown in the inset of **f** is collected at 30-ID, APS with  $h\nu=23.71$  keV.

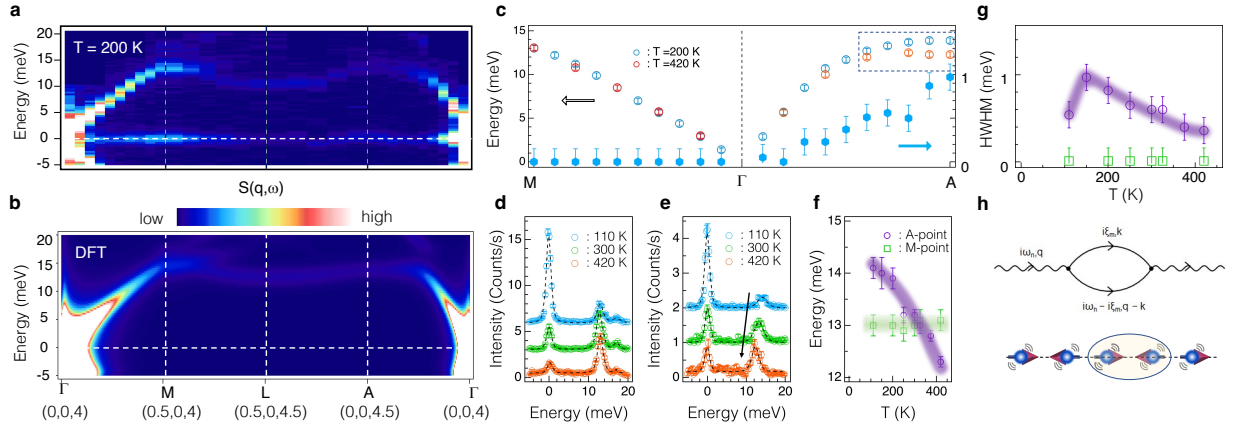


**Figure 3: Giant phonon anomalies near the charge dimerization wavevectors.** **a** and **b**, experimental and DFT  $S(Q, \omega)$  along the  $\Gamma(0, 0, 4)$ - $M(0.5, 0, 4)$ - $L(0.5, 0, 4.5)$ - $A(0, 0, 4.5)$ - $\Gamma(0, 0, 4)$  direction. As described in Methods, the IXS intensity is dominated by the lattice distortions along the crystal  $c$ -axis. The IXS data shown in **a** were collected at 200 K. **c**, Extracted phonon dispersion along the  $M$ - $\Gamma$ - $A$  direction at 200 (cyan) and 420 K (orange). The dashed rectangle highlights the temperature dependent phonon energy renormalization near the A point. **d** and **e**, temperature dependent IXS spectra at the M and A point. Dashed curves are fittings of the experimental data (see Methods). Blue, green and orange circles represent 110, 300 and 420 K, respectively. **f**, Temperature dependence of the fitted phonon peak positions at the A (open purple circles) and M (open green squares) point. **g**, Temperature dependence of the fitted phonon peak width at the A (open purple circles) and M (open green squares) point. **h**, Dynamical spin-phonon coupling. Top panel shows the second-order Feynman diagram for the phonon self-energy. Dashed and solid lines represent the phonon and magnon Green's functions, respectively.  $i\omega_n$  and  $i\xi_m$  are bosonic Matsubara frequencies. Bottom panel shows a schematic of the dynamical spin-phonon coupling in an effective 1-dimensional spin chain with A-AFM. The spin-phonon coupling induces strong the phonon self-energy effects and yields a phonon-energy hardening and phonon-linewidth broadening near the charge dimerization A-point (see Supplementary Materials). The vertical error bars shown in **c-f** represent 1-standard deviation from either Poissonian statistics or least-squares fitting. The vertical error bars shown in **g** represent the experimental step size that is about 3 times larger than the fitting error bars.

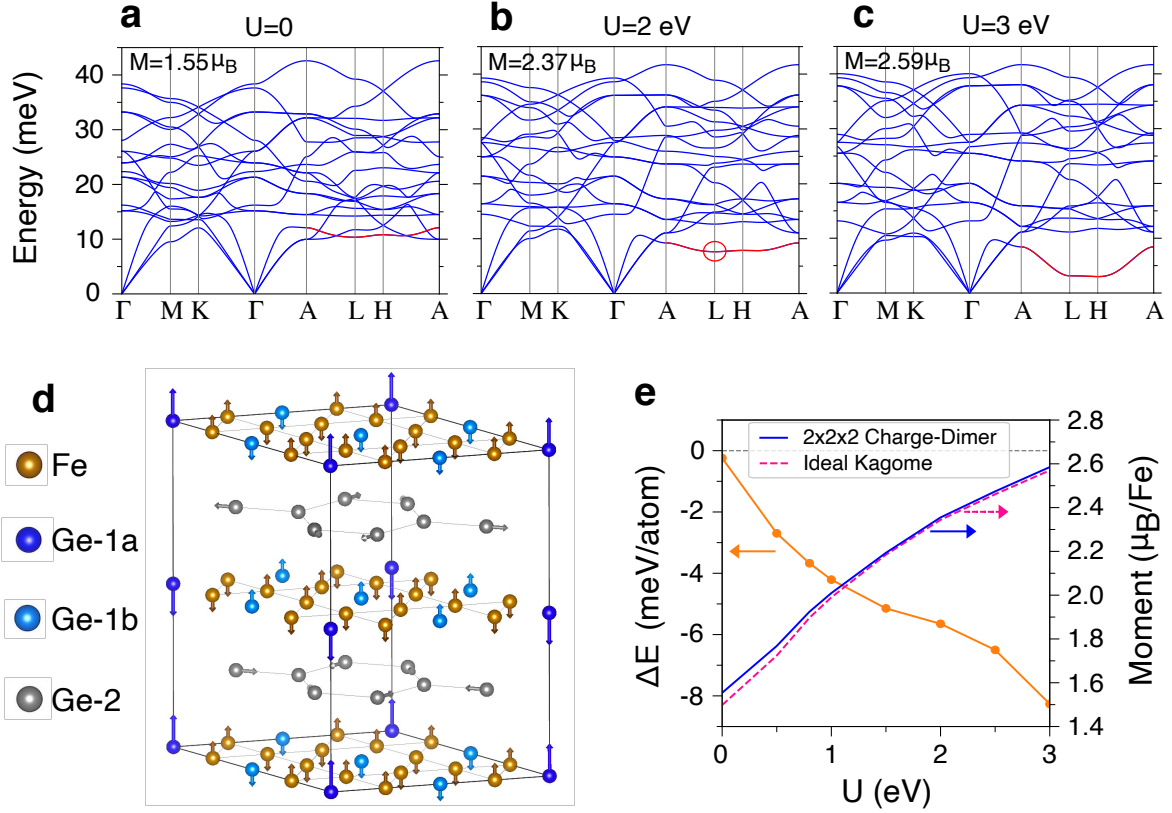


**Figure 4: Spin-polarization-induced charge-dimerized  $2\times 2\times 2$  superstructure in FeGe.** a,b,c, The DFT+ $U$  calculated phonon spectra of FeGe in the AFM phase as increasing Hubbard  $U$ . The phonon spectra are plotted with respect to the non-magnetic BZ of FeGe. The calculated ordered magnetic moments per Fe atom,  $M$ , are  $1.55$ ,  $2.27$  and  $2.59 \mu_B$  for  $U=0$ ,  $2$  and  $3$  eV, respectively. The calculated  $M$  at  $U=0$  eV is closer to the experimental value. The red curve corresponds to the experimentally observed phonon modes which show the most dramatic change as the spin-polarization is enhanced. The red circles highlight the  $B_{1u}$  phonon mode at the L-point, which has the lowest energy along the **A-L-H-A** direction. **d**, The equal phase and amplitude superposition of the  $B_{1u}$  modes at the three equivalent L-points yields a charge-dimerized  $2\times 2\times 2$  superstructure. The arrows indicate the movements of Fe and Ge atoms. In kagome layers, Fe and Ge atoms move out-of-plane to form dimers along c-axis. Ge-1a (blue) and Ge-1b (light blue) have out-of-phase vibrations. Ge-1a has larger movement than Ge-1b. The honeycomb layers of Ge-2 (grey) atoms show in-plane Kekulé-type distortions. **e**, Left y-axis shows the DFT+ $U$  calculated energy difference between the charge-dimerized  $2\times 2\times 2$  superstructure and the ideal Kagome phase,  $\Delta E = E_{\text{Charge-Dimer}} - E_{\text{Kagome}}$ . Right y-axis shows the calculated ordered magnetic moment of

the charge-dimerized  $2\times 2\times 2$  superstructure (blue solid) and ideal Kagome (red dashed) phases, respectively. The magnetic moments are enhanced by  $0.01\sim 0.05 \mu_B/\text{Fe}$  by forming the charge-dimerized  $2\times 2\times 2$  superstructure.